Journal of Spacecraft and Rockets

VOLUME 2 JULY-AUGUST 1965 NUMBER 4

Analysis of Flow Separation Effects on the Dynamics of a Large Space Booster

LARS-ERIC ERICSSON[*] AND J. PETER REDING[†]
Lockheed Missiles and Space Company, Sunnyvale, Calif.

The next generation of manned space boosters, the Saturn-Apollo family, presents the structural dynamicist with the unique situation of having to analyze the response of vehicles that are to a great extent submerged in separated flow. The problem is further aggravated by the occurrence of maximum dynamic pressure in the transonic and low-supersonic speed ranges wherein flow separations completely dominate the aerodynamics. Quasi-steady aerodynamic techniques are used to ascertain the effects that the various types of flow separation have on the aerodynamic damping of the Saturn I-Apollo launch vehicle. A single degree-of-freedom analysis of each of the three lowest bending modes is presented. The analysis uses as an input a lumped-force representation of the experimentally obtained static load distribution. The resulting aerodynamic damping distribution can be related directly to the static-load distribution, and the designer can trace any adverse damping effects back to the static-load distribution and thus to the vehicle geometry. The net aerodynamic damping for part or all of the vehicle, obtained by integration of the damping distribution, agrees well, in general, with available experimental results.

Nomenclature

A = axial force, kg, coefficient $C_A = A/(\rho U^2/2)S$
d = rocket diameter, m
D_{ref} = reference length, m
D = aerodynamic damping derivative
$f(t)$ = driving function, m/sec^2
i = imaginary number $(-1)^{1/2}$
K = aerodynamic stiffness derivative
L = longitudinal distance, m
M = Mach number
M_A = axial force moment, kg-m, coefficient $C_{mA} = M_A/(\rho U^2/2)SD_{\mathrm{ref}}$
$\tilde{m}$ = generalized mass, kg-sec^2/m
N = normal force, kg, coefficient $C_N = N/(\rho U^2/2)S$
$P(t)$ = generalized force, kg
p = static pressure, kg/m^2, coefficient $C_P = (p - p_\infty)/(\rho U^2/2)$
$q(t)$ = normalized coordinate, m
S = reference area, m^2
t = time, sec
U = velocity, m/sec
X = horizontal coordinate, m
Z = vertical coordinate, m
z = relative deflection, m
α = angle-of-attack, radians or degrees
β = equivalent spike deflection angle, radians or degrees
δ = boundary-layer thickness, m
Δ = difference
ρ = air density, kg-sec^2/m^4
ω = free-free bending frequency, rad/sec
ζ = structural damping, fraction of critical
ζ_s, ζ_a = aerodynamic damping, fraction of critical
θ = rotation angle, rad or deg
φ = normalized modal deflection
φ' = normal mode slope

Subscripts

a = attached flow
b = base, also buffeting flow
C = cylinder
QS = quasi-steady
s = separated flow
t = total
∞ = undisturbed flow
0 = at $\alpha = 0$

Superscripts

i = induced, e.g., $\Delta^i C_N$ = separation induced normal force

Introduction

WITH the advent of manned space flight, astronaut escape systems, blunt nose cones, and steep interstage flares have become characteristic of space boosters. Each geometric characteristic complicates the problems for the aerodynamicist and structural dynamicist by producing large regions of flow separation, which dominate the aerodynamic loading over the vehicle in the transonic and low-supersonic

---

Presented as Preprint 64-482 at the 1st AIAA Annual Meeting, Washington, D. C., June 29–July 2, 1964; revision received November 16, 1964. The results reported herein were obtained in a study conducted at the Lockheed Missiles and Space Company for the George Marshall Space Flight Center, NASA, under Contract NAS 8-5338.

[*] Senior Staff Engineer. Associate Fellow Member AIAA.

[†] Senior Dynamics Engineer. Member AIAA.

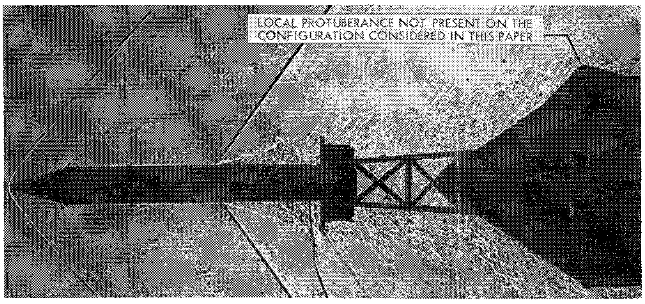

a) Supersonic flow field at $M = 1.43$ tower on ($\alpha = 0$)

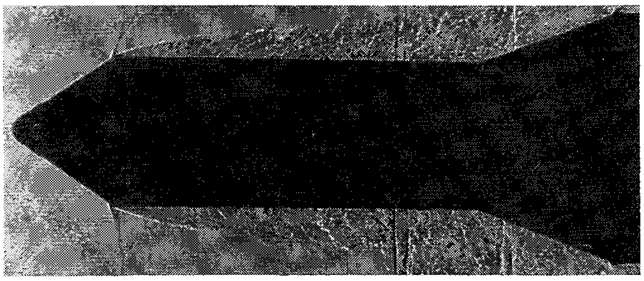

b) Subsonic flow field at $M = 0.9$ tower off ($\alpha = 0$)

Fig. 1 Shadowgraphs of transonic flow fields.

speed ranges wherein the vehicle experiences maximum dynamic pressure. The static loads as well as the buffeting force input from the separated flow can be determined by wind tunnel tests of a rigid model. The remaining information needed, the aerodynamic damping, is more difficult to obtain, however. To simulate elastic vehicle response in a wind tunnel test is very complicated, and the results of this expensive test may still be of limited value due to wind tunnel noise and model-mount interference. Furthermore, the elastic model necessitates a lead time of as much as one year, and post test design changes in the full-scale vehicle required for various reasons result in the test data being of little help.

These problems were recognized at the NASA Marshall Space Flight Center (MSFC) in connection with the design of the Saturn I-Apollo launch vehicle. Because similar problems had been encountered on the Agena ascent vehicle,[1, 2] Lockheed Missiles and Space Company (LMSC) was engaged by the NASA MSFC to develop analytical means for prediction of full-scale vehicle dynamics. The method is founded on quasi-steady techniques and uses static experimental data as an input.

Method of Approach

The loads occurring in a separated flow region fall generally into two categories: 1) those due to the effect of forebody attitude and relative displacement on the flow separation; and 2) those due to local attitude of the submerged body element. For the former loads there is a time lag before a perturbation of the forebody has altered the submerged-body loads, which may cause a phase shift in the dynamic case such that statically stabilizing loads become dynamically destabilizing. The latter loads are dependent upon the instantaneous change in local attitude and displacement, and are, for large regions of separated flow, significantly smaller than the former.

In what follows, the aerodynamic loads in the various separated flow regions on the Saturn I-Apollo launch vehicle are analyzed. It is shown that a rational partition of the static loads into local and forebody-dependent components can be made, based upon the velocity deficit in the separated flow region. These static forces are converted to unsteady loads by quasi-steady methods. The quasi-steady force is essentially the static force modified to account for slow perturbations from the static (steady-state) condition.

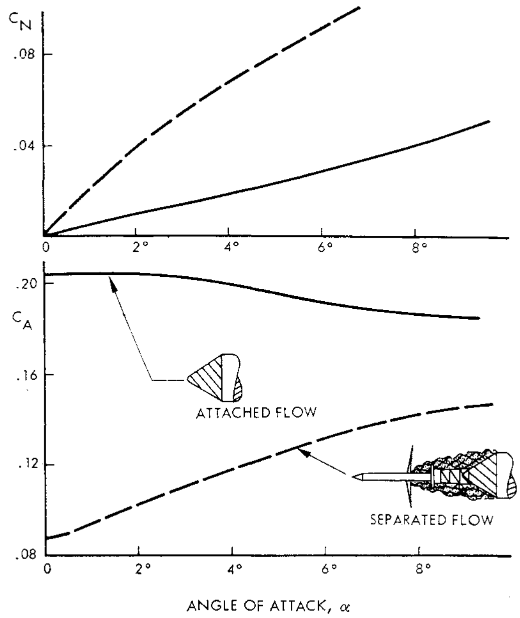

a) Effect of escape rocket on command module forces at $M = 1.0$

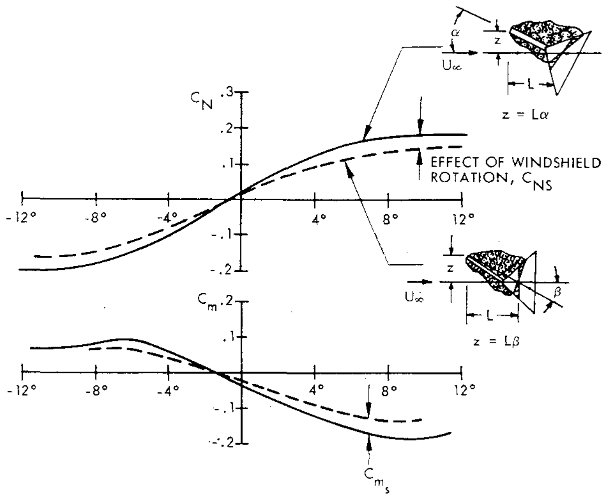

b) Comparison of angle-of-attack and spike deflection effects of $M = 2.93$

Fig. 2 Wake-induced aerodynamic characteristics.

Aerodynamic Characteristics

Figure 1a is a shadowgraph of the flow field in the vicinity of the Apollo escape rocket and command module, showing the large region of flow separation produced by the escape-rocket wake. Figure 1b illustrates the occurrence at the command module shoulder of extensive flow separation caused by the blunt (33°) conical command module at subsonic Mach number, $M = 0.9$. These two types of flow separation drastically alter the static force loadings over the submerged afterbodies.[3] The impingement of the escape-rocket wake on the command module produces the most severe separated flow effect, very similar to that obtained with a flow separation spike. Furthermore, the steep interstage flares produce their own regions of flow separation, both subsonically and supersonically.

Spiked-Induced Separation

Figure 2a shows how the flow separation from the escape rocket reduces the axial force at $\alpha = 0$ (due to the reduced average velocity in the wake) while increasing the normal force derivative and producing a more stable pitching moment. The latter effects result from translating the wake over the submerged body, thus exposing the windward side to rapidly increasing velocities and the leeward side to reduced velocities. The wake-translating effects of α and of spike deflection angle β should be the same (Fig. 2b) since the relative spike tip translation is the same ($z = \alpha L = \beta L$ for small angles). Thus, the difference between the α- and β-characteristics is due to rotating the windshield through the angle α. That is, two force derivatives are generated with angle of attack: an induced force $\Delta^i C_{N\beta}$, proportional to the effective spike deflection angle β, and a local rotational force $C_{N_{\alpha}^{s}}$ due to the attitude α_s of the windshield. Lacking experimental data for deflected escape rocket and tower, the effect of local attitude may be assessed by considering the command module pitched in the reduced dynamic-pressure field of the wake. The reduced axial force on the command module is a direct measure of the dynamic-pressure deficit. Thus,

$$C_{N_{\alpha}^{s}}/C_{N_{\alpha}^{a}} = q_s/q_\infty = C_{A0s}/C_{A0a} \tag{1}$$

where C_{A0a} is measured with tower off, and C_{A0s} is measured with tower on. The induced derivative due to wake-source translation is

$$\Delta^i C_{N_{\alpha}^{s}} = \Delta^i C_{N_\beta} = C_{N_{\alpha\text{total}}} - C_{N_{\alpha}^{s}} \tag{2}$$

Figure 3 shows how these command module forces vary with Mach number. When the escape-rocket disk is removed, a further complication is introduced, viz. the wake-directing capability of the escape-rocket flare. Figure 3b illustrates how the wake of a directing spike tip is moved downward an amount Δz proportional to the wake source attitude θ_s. The total wake-induced derivative is, therefore,

$$\Delta^i C_{N_{\alpha}^{s}} = \Delta^i C_{N_\beta} + \Delta^i C_{N_{\theta}^{s}} \tag{3}$$

The disk-off wake-translation effect may be evaluated from the disk-on data by adjusting for wake-size effects. Since the $\alpha = 0$ axial force reduction is indicative of wake size, the disk-off derivative may be computed as follows:

$$(\Delta^i C_{N_\beta})_{\text{disk off}}/(\Delta^i C_{N_\beta})_{\text{disk on}} = (\Delta^i C_{A0})_{\text{disk off}}/(\Delta^i C_{A0})_{\text{disk on}} \tag{4}$$

where $\Delta^i C_{A0} = C_{A0a} - C_{A0s}$. The remaining induced derivative $\Delta^i C_{N_{\theta}^{s}}$ is simply $\Delta^i C_{N_{\theta}^{s}} = \Delta^i C_{N_{\alpha}^{s}} - \Delta^i C_{N_\beta}$; Fig. 3b shows the Mach number dependence of these local and induced derivatives. The local and induced command-module axial force moments are obtained similarly.

The wake from the escape rocket, after impinging on the command module, reattaches on the service module aft of

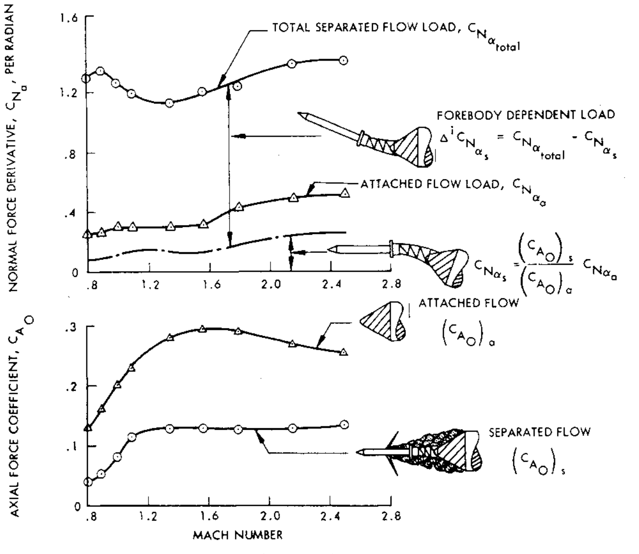

a) Disk on

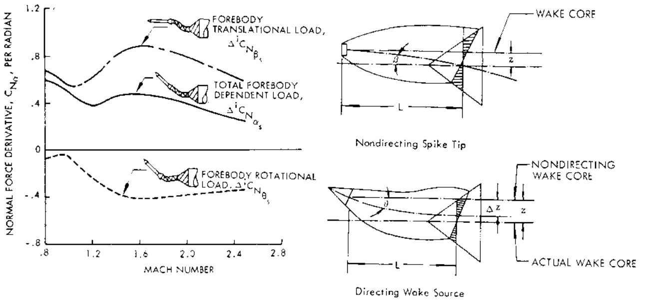

b) Disk off

Fig. 3 Command-module forebody-dependent and local loads at $\alpha = 0$.

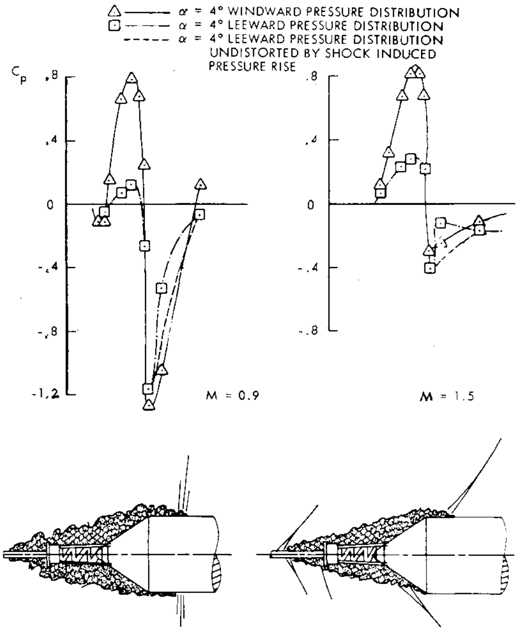

a) Pressure distribution at $\alpha = 4°$

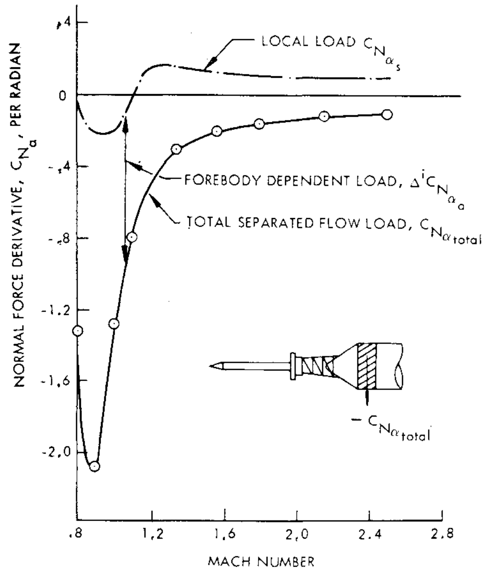

b) Shoulder loading at $\alpha = 0$ (tower and disk on)

Fig. 4 Command-module shoulder forces.

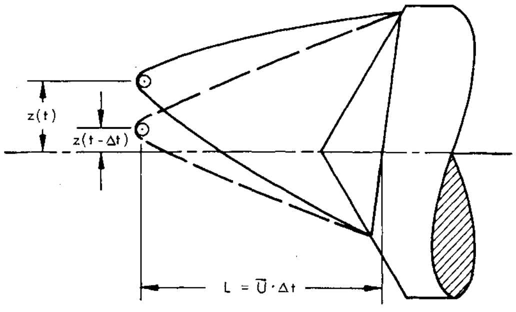

Fig. 5 Sketch of quasi-steady spike wake.

the shoulder. The pressure distributions of Fig. 4a indicate that a negative shoulder loading is generated by the reattaching wake, with the major contribution coming from the leeward side through greatly reduced negative pressures due to the upstream effects of the pressure rise at reattachment. The loading induced by the wake-source translation is always negative, whereas the local load may be either positive or negative depending on the initial ($\alpha = 0$) wake configuration (Fig. 4b). In comparing these loadings with the command-module loadings in Fig. 3, it can be seen that the negative shoulder load will dominate at subsonic and sonic speeds, whereas at supersonic speeds the positive command-module load is dominant.

The spike-induced quasi-steady force can be derived in a straightforward manner. For a thin spike only the location of the spike tip is important. In Fig. 5 the spike tip is describing translatory oscillations relative to the conical windshield, the relative displacement z being a function of time. At time t the spike tip has the lateral displacement $z(t)$. The wake impinging upon the windshield at time t, however, was generated a time increment Δt earlier, when the spike tip had the relative displacement $z(t - \Delta t)$. This is the quasi-steady spike position, i.e., the static spike position for which the wake will impinge at the same location on the windshield as in the nonstationary case. The time lag is the time required for the wake to travel from the spike tip to the windshield $t = L/\bar{U}$. A representative average velocity $\bar{U}$ can be derived from the dynamic-pressure deficit given by Eq. (1):

$$\bar{U}/U = (q_s/q_\infty)^{1/2} \tag{5}$$

Since the attitude of the spike tip has no effect on the lateral position of the wake, the quasi-steady force induced by the lateral wake movement is

$$\Delta^i C_{QS} = (\partial C_{N_s}/\partial z) z(t - \Delta t)$$

$$(\partial C_{N_s}/\partial z) = (1/L)\Delta^i C_{N_\beta} \tag{6}$$

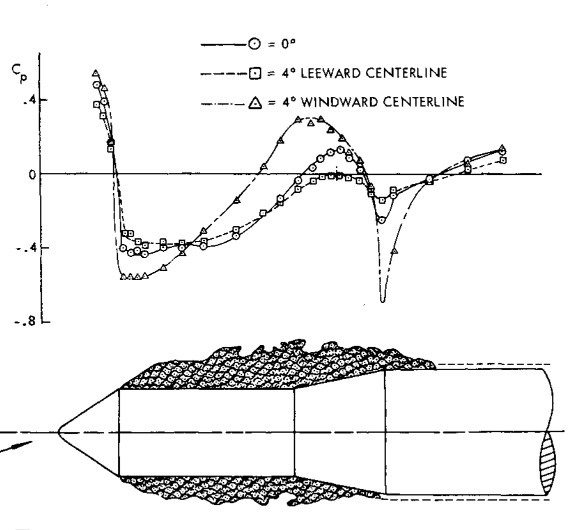

Fig. 6 Forebody pressure distribution with escape system removed at $M = 0.9$.

The remaining quasi-steady force on the windshield is

$$C_{QS} = \partial C_{N_s}/\partial \alpha_s[\theta(t) + \dot{Z}(t)/U] \tag{7}$$

where θ and $\dot{Z}$ are the local instantaneous attitude and translatory velocity of the windshield.‡

On the Saturn I-Apollo configuration, the escape-rocket disk corresponds directly to the spike tip. There is some

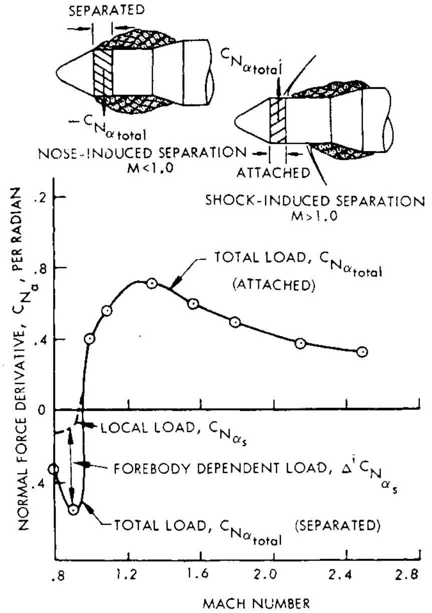

a) Command-module shoulder loads

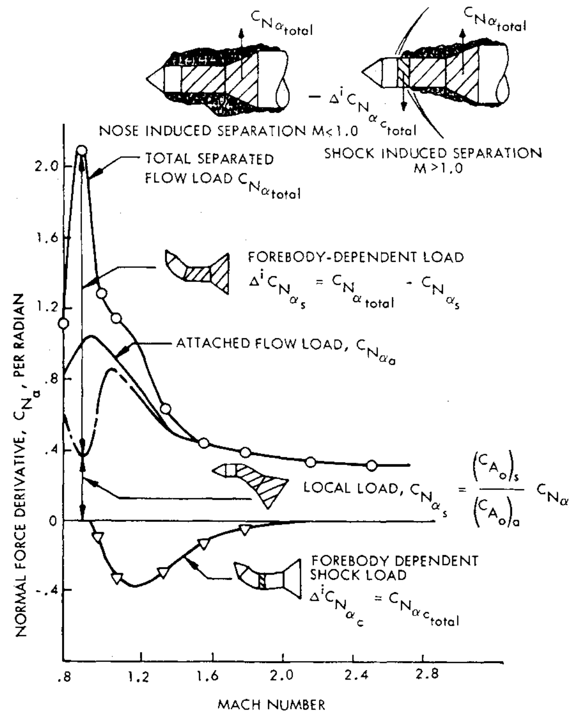

b) Cylinder and flare loads

Fig. 7 Forces in nose-induced separation at $\alpha = 0$ (tower off).

---

‡ In studying Fig. 5 it is apparent that the nonsteady wake is inclined relative to the quasi-steady wake. However, the unsteady wake also has a translatory velocity relative to the quasi-steady wake, negating the effect of the inclined wake axis.

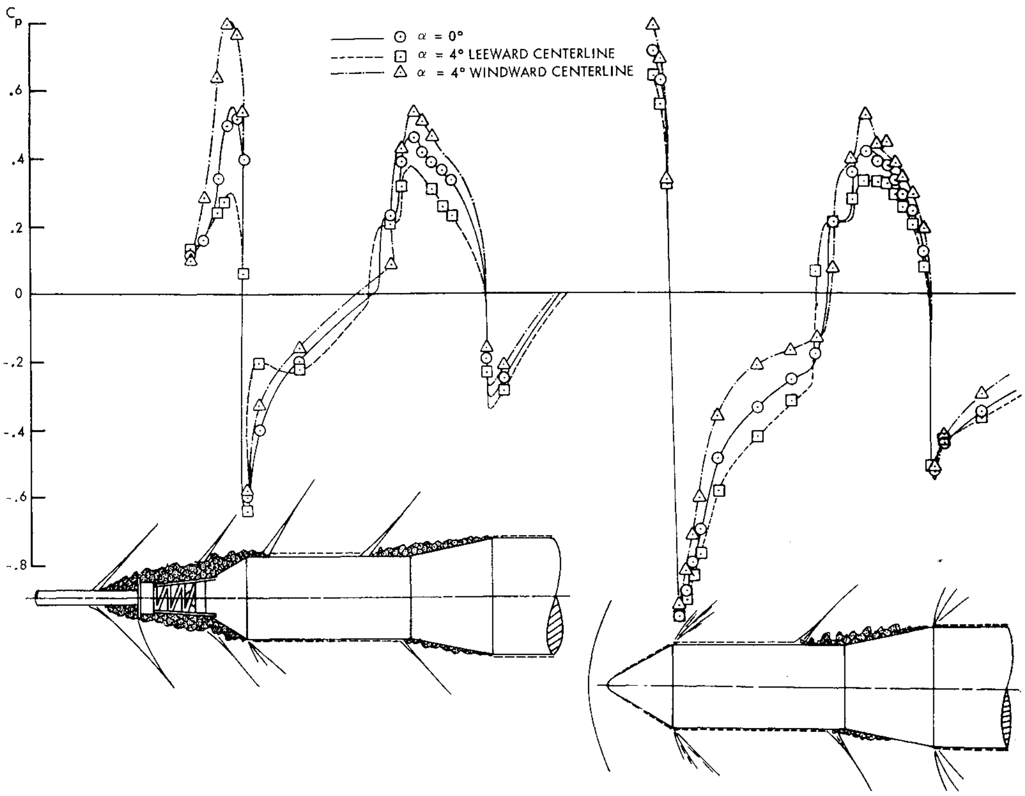

a) Tower on, $M = 1.2$ b) Tower off, $M = 1.1$

Fig. 8 Forebody supersonic pressure distribution.

influence of the escape rocket on the leeward portion of the disk wake at angle-of-attack. However, this effect is small, and Eq. (6) sufficiently describes the disk wake-induced quasi-steady forces on the command module and forward service module. When the disk is removed, the escape-rocket flare attitude has a directing influence on the wake. Thus Eq. (6) is modified as follows:

$$\Delta^i C_{QS} = \frac{\partial C_{N_s}}{\partial z}\, z(t - \Delta t) + \frac{\partial C_{N_s}}{\partial \theta_s}\, \theta_s(t - \Delta t) \qquad (8)$$

where θ_s is the attitude of the rocket flare, and $\partial C_{N_s}/\partial \theta_s < 0$ is the directing effect of the rocket flare.

Nose-Induced Separation

When the escape system is removed, the flow separates off the shoulder of the blunt command module at subsonic Mach numbers (Fig. 1b). The boundary layer cannot negotiate the steep, adverse pressure gradient over the forward service module without separating. This nose-induced separation is akin to the thin airfoil leading-edge separation with its so-called long bubble.[4] Figure 6 shows that the pressure is constant in the separated flow region extending to the aft service module and flare, where the reattachment process occurs. At angle-of-attack the windward boundary layer on the command module is strengthened and made thinner, and can therefore withstand a greater adverse pressure gradient. This, together with the added constraint of the external flow, permits the windward side pressures to approach attached flow values, and the command-module shoulder pressure becomes more negative. On the leeward side, the effect is opposite but less drastic. The resulting negative shoulder load is proportional to the forebody crossflow, which in lumped form can be represented by the crossflow at the shoulder. On the aft service module and flare the increased velocities in the windward side of the wake produce increased pressures approaching attached flow values. Again, on the leeward side the effect is the opposite. The effect of local attitude on the flare force $C_{N_\alpha}{}^s$ is determined by the drag reduction, Eq. (1). The remainder of the flare force $\Delta^i C_{N_\alpha}{}^s$ is induced by the wake changes, Eq. (2), and is determined by the crossflow at the command-module shoulder. The same ratio between local and induced loads is used for the service module loading. Figure 7 shows these forces, demonstrating the large effect of the nose-induced separation at subsonic speeds. At supersonic speeds the nose-induced separation disappears, and instead, a small separated flow region caused by the flare shocks appears. The pressure distribution in Fig. 6 shows that a negative load exists aft of the flare shoulder. It is similar to the negative shoulder load obtained aft of the command module in the presence of the escape system and, therefore, is treated in the same manner.

The forces $\Delta^i C_{N_s}$ induced in the separated flow are determined by the crossflow at the command-module shoulder. In the quasi-steady case a time lag Δt occurs before this crossflow has affected the separated flow region aft of the shoulder, i.e.,

$$\Delta^i C_{QS} = \Delta^i C_{N_\alpha}{}^s[\theta_N(t - \Delta t) + \dot{Z}_N(t - \Delta t)/U] \qquad (9)$$

where θ_N and $\dot{Z}_N$ are the local attitude and translatory velocity of the command-module shoulder. The time lag Δt is again assessed by accounting for the velocity deficit in the wake, evidenced by the flare drag reduction [see Eqs. (1) and (5)].

Shock-Induced Separation

The pressure distributions in Fig. 8 indicate that a region of shock-induced separation occurs forward of the interstage flare joining the service module with the S-IV stage. The separation induces a negative cylinder load at the start of separation due to the differential windward and leeward shock position. The positive loads induced on the cylinder and flare immediately aft of the shocks result not only from

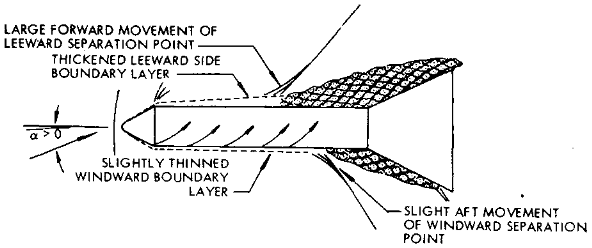

a) **Effect of boundary-layer thickness**

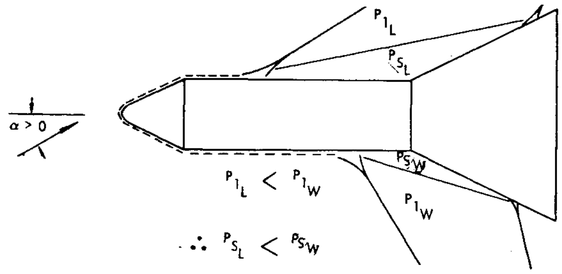

b) **Effect of detached shock angle**

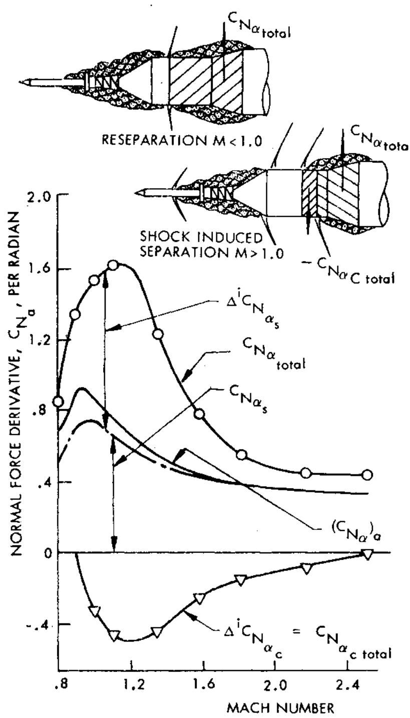

c) **Local and forebody-dependent aft cylinder and flare loads at $\alpha = 0$ (tower and disk on)**

Fig. 9 Shock-induced separation.

the differential shock position but also from the difference in windward and leeward side shock strength. The extent of the separation forward of the flare is proportional to the boundary-layer thickness δ immediately ahead of the separation.[5] The effect of angle-of-attack is to increase the leeward side boundary-layer thickness and decrease that of the windward side (Fig. 9a). Consequently, the extent of the separation is increased on the leeward side and decreased on the windward side, resulting in a negative cylinder load (due to differential shock position), and a positive flare load (due to the changed separated flow extent). Moreover, at angle-of-attack, the windward shock gives a higher pressure rise than the leeward shock (Fig. 9b), with a correspondingly higher pressure in the windward separated flow region than on the leeward side, producing positive aft body loads on the cylinder and flare. The negative cylinder load is all induced and dependent upon the forebody influence on the boundary layer at separation. The effect of local flare attitude $C_{N_{\alpha s}}$ is assessed as before. The remainder of the flare force $\Delta^i C_{N_{\alpha s}}$ is induced by the separation. One part $\Delta^i C_{N_{\alpha s1}}$ is determined by the forebody crossflow ahead of the separation, and the other part $\Delta^i C_{N_{\alpha s2}}$ is dependent upon the local crossflow at the shock location. The cylinder-flare load, with its local and induded components, is shown in Fig. 9c. The figure indicates that a definite flare-induced separation exists even at subsonic speeds (produced by the tower-wake reattachment shocks). When the separated flow reattaches on the cylinder aft of the flare a negative shoulder load is obtained as described earlier for the nose-induced separation.

The quasi-steady boundary-layer thickness at the separation point at time t is dependent upon local crossflow upstream at earlier time instants $t - \Delta t_n$, where Δt_n is the time required for the boundary layer at the separation point to respond to the upstream crossflow change. The forebody normal force distribution is a measure of the local crossflow effects, and, therefore, the forebody crossflow is represented in lumped form by the crossflow at the aerodynamic center X_{AC} of the forebody attached flow loading. Thus, the quasi-steady boundary-layer thickness at the separation point at time t is determined by the local crossflow at X_{AC} at time $t - \Delta t$, where $\Delta t = L/\bar{U}$ is the time required for the crossflow effect to be transmitted through the boundary layer the distance $L = X_{AC} - X_C$ down to the separation point X_C. $\bar{U}$ is the convection speed, which in a turbulent boundary layer at transonic and low supersonic speeds is $\bar{U} = 0.8U$.[6] (The average velocity defined earlier in the separated flow regions gives $\bar{U} = 0.87U$ for a $\frac{1}{7}$th power profile.) Thus, the quasi-steady force at X_C is

$$(\Delta^i C_{QS})_C = \Delta^i C_{N_{\alpha C}} \bar{\alpha}_{AC}(t - \Delta t) \tag{10}$$

The term $\bar{\alpha}_{AC}$ is the crossflow angle at X_{AC} defined by the local attitude θ_{AC} and translatory velocity $\dot{Z}_{AC}$, i.e., $\bar{\alpha}_{AC} = \theta_{AC} + \dot{Z}_{AC}/U$. Likewise, the two quasi-steady flare force components at X_s are defined as follows: 1) force induced by the shock movement

$$(\Delta^i C_{QS})_1 = \Delta^i C_{N_{\alpha s1}} \bar{\alpha}_{AC}(t - \Delta t - \Delta t_1) \tag{11}$$

Δt_1 is the additional time lag through the separated flow region $(X_C - X_s)$, i.e., $\Delta t_1 = (X_C - X_s)\bar{U}_1$, where $\bar{U}_1$ is the average wake velocity and 2) force induced by the shock angle

$$(\Delta^i C_{QS})_2 = \Delta^i C_{N_{\alpha s2}} \bar{\alpha}_C(t - \Delta t_1) \tag{12}$$

$\bar{\alpha}_C$ is the crossflow angle at the shock location X_C, i.e., $\bar{\alpha}_C = \theta_C + \dot{Z}_C/\bar{U}$. The quasi-steady induced negative load on the flare shoulder is treated the same way as the positive flare load, the only difference being the additional time lag to cover the distance from flare to shoulder load. The shock-induced quasi-steady force is difficult to assess, and it is fortunate that the forces always appear in pairs, a negative cylinder load followed by a positive flare load, resulting in a moderate net effect.

Vehicle Dynamics

The dynamics of the elastic vehicle are analyzed for single degree-of-freedom oscillations in one bending mode.

Equation of Motion

The equation of motion can be written in the following form using standard notations:

$$\bar{m}[\ddot{q}(t) + 2\zeta\omega\dot{q}(t) + \omega^2 q(t)] = P(t) \tag{13}$$

The generalized force $P(t)$ is given by the virtual work done by the aerodynamic forces on the vehicle§:

$$P(t) = \int \frac{dN}{dX}\,\varphi(X)dX + \int \frac{dM_A}{dX}\,\varphi'(X)dX \qquad (14)$$

There are three different types of generalized force

$$P(t) = P_s(t) + P_a(t) + P_b(t) \qquad (15)$$

Both $P_b(t)$ and $P_a(t)$ can be defined by well-established methods. $P_b(t)$ is a forcing function, a random function for the case of buffeting forces. $P_a(t)$, the generalized force in attached flow, can be estimated by use of first-order theory.[7] $P_s(t)$ is, however, more difficult to determine, and the main effort here is devoted to describing how this force can be estimated by the use of static experimental data. In Fig. 10 it is assumed that the flow is attached aft of body station X_a. The forces in the separated flow forward of X_a are represented in lumped form. In general, the force N_s and the axial force moment M_s will be dependent not only upon the local angle-of-attack α_s but also upon the angle-of-attack α_N at the nose and the relative displacement $z = -(Z_N - Z_s)$ between nose and frustum. For small deflections one may write N_s in the following form (a similar expression is obtained for M_s):

$$N_s = \frac{\rho U^2}{2} S \left\{ \frac{\partial C_N}{\partial \alpha_N}\,\alpha_N + \frac{\partial C_N}{\partial z}\,z + \frac{\partial C_N}{\partial \alpha_s}\,\alpha_s \right\} \qquad (16)$$

In the unsteady case α_N and Z_N in $-(Z_N - Z_s)$ will be the values at a time Δt earlier than the instantaneous value for α_s, i.e.,

$$N_s(t) = \frac{\rho U^2}{2} S \left\{ \frac{\partial C_{N_s}}{\partial \alpha_s}\,\alpha_s(t) + \frac{\partial C_{N_s}}{\partial \alpha_N}\,\alpha_N(t - \Delta t) - \frac{\partial C_{N_s}}{\partial z}\,[Z_N(t - \Delta t) - Z_s(t)] \right\} \qquad (17)$$

Δt is the time required for the force N_s to respond to changes in α_N and Z_N. For the elastic vehicle in Fig. 10, $\alpha = \theta + \dot{Z}/U$, $Z = -\varphi(X)q(t)$, and $\theta = \varphi'(X)q(t)$. The contribution to the generalized force $P_s(t)$ from the force N_s and moment M_s of the frustum in the separated flow can then be expressed as follows, using the lumped version of Eq. (14):

$$\begin{aligned} P_s(t) = {} & \frac{\rho U^2}{2} S\varphi(X_s) \left\{ \frac{\partial C_{N_s}}{\partial \alpha_s} \left[\varphi'(X_s)q(t) - \varphi(X_s)\,\frac{\dot{q}(t)}{U} \right] + \right. \\ & \frac{\partial C_{N_s}}{\partial \theta_N}\,\varphi'(X_N)q(t - \Delta t) - \frac{\partial C_{N_s}}{\partial(\dot{Z}_N/U)}\,\varphi(X_N)\,\frac{\dot{q}(t - \Delta t)}{U} + \\ & \left. \frac{\partial C_{N_s}}{\partial z}\,[\varphi(X_N)q(t - \Delta t) - \varphi(X_s)q(t)] \right\} + \\ & \frac{\rho U^2}{2} SD_{\text{ref}}\varphi'(X_s) \left\{ \frac{\partial C_{m_s}}{\partial \alpha_s} \left[\varphi'(X_s)q(t) - \varphi(X_s)\,\frac{\dot{q}(t)}{U} \right] + \right. \\ & \frac{\partial C_{m_s}}{\partial \theta_N}\,\varphi'(X_N)q(t - \Delta t) - \frac{\partial C_{m_s}}{\partial(\dot{Z}_N/U)}\,\varphi(X_N)\,\frac{\dot{q}(t - \Delta t)}{U} + \\ & \frac{\partial C_{m_s}}{\partial z}\,[\varphi(X_N)q(t - \Delta t) - \varphi(X_s)q(t)] \end{aligned} \qquad (18)$$

The force on the nose is dependent only on the local angle-of-attack. The force on the shoulder aft of the frustum, where the separated flow reattaches on the cylinder, is composed the same way as the force on the frustum. How the time lag Δt is evaluated has been discussed earlier.

The term $P_s(t)$ in this form, Eq. (18), together with Eqs. (13) and (15), can be used in a real-time analytical simulation of the vehicle ascent. Equation (18) can, however, be simplified further, as the structural stiffness usually is one order of magnitude larger than the aerodynamic stiffness, and the structural and aerodynamic damping as a rule are two orders of magnitude less than critical. That is, the vehicle may be assumed to oscillate with the natural free-free bending frequency ω and $q(t)$ can be expressed as follows:

$$q(t - \Delta t) \approx e^{-i\omega\Delta t}q(t) = \cos(\omega\Delta t)q(t) - \sin(\omega\Delta t)[iq(t)] \qquad (19)$$

where $\dot{q}(t) \approx \omega[iq(t)]$. (This assumption also makes $2\zeta\omega\dot{q}(t)$ equivalent to $ig\omega^2q(t)$ in Eq. (13), where $2\zeta = g$.) Equation (18) can now be written

$$P_s(t) = \frac{\rho U^2}{2} S \left[K_s q(t) + D_s\,\frac{\dot{q}(t)}{U} \right]$$

$$\begin{aligned} K_s = {} & \varphi(X_s) \left\{ \frac{\partial C_{N_s}}{\partial \alpha_s}\,\varphi'(X_s) + \frac{\partial C_{N_s}}{\partial \theta_N}\,\varphi'(X_N)\cos(\omega\Delta t) - \right. \\ & \frac{\partial C_{N_s}}{\partial(\dot{Z}_N/U)}\,\varphi(X_N)\,\frac{\omega}{U}\sin(\omega\Delta t) + \frac{\partial C_{N_s}}{\partial z}\,[\varphi(X_N)\cos(\omega\Delta t) - \\ & \left. \varphi(X_s)] \right\} + D_{\text{ref}}\varphi'(X_s) \left\{ \frac{\partial C_{m_s}}{\partial \alpha_s}\,\varphi'(X_s) + \right. \\ & \frac{\partial C_{m_s}}{\partial \theta_N}\,\varphi'(X_N)\cos(\omega\Delta t) - \frac{\partial C_{m_s}}{\partial(\dot{Z}_N/U)}\,\varphi(X_N)\,\frac{\omega}{U}\sin(\omega\Delta t) + \\ & \left. \frac{\partial C_{m_s}}{\partial z}\,[\varphi(X_N)\cos(\omega\Delta t) - \varphi(X_s)] \right\} \end{aligned} \qquad (20)$$

$$\begin{aligned} D_s = {} & -\varphi(X_s) \left\{ \frac{\partial C_{N_s}}{\partial \alpha_s}\,\varphi(X_s) + \left[\frac{\partial C_{N_s}}{\partial \theta_N}\,\varphi'(X_N) + \right. \right. \\ & \left. \left. \frac{\partial C_{N_s}}{\partial z}\,\varphi(X_N) \right] \frac{U}{\omega}\sin(\omega\Delta t) + \frac{\partial C_{N_s}}{\partial(\dot{Z}_N/U)}\,\varphi(X_N)\cos(\omega\Delta t) \right\} - \\ & D_{\text{ref}}\,\varphi'(X_s) \left\{ \frac{\partial C_{m_s}}{\partial \alpha_s}\,\varphi(X_s) + \left[\frac{\partial C_{m_s}}{\partial \theta_N}\,\varphi'(X_N) + \right. \right. \\ & \left. \left. \frac{\partial C_{m_s}}{\partial z}\,\varphi(X_N) \right] \frac{U}{\omega}\sin(\omega\Delta t) + \frac{\partial C_{m_s}}{\partial(\dot{Z}_N/U)}\,\varphi(X_N)\cos(\omega\Delta t) \right\} \end{aligned}$$

Similarly, $P_a(t)$ may be expressed as

$$P_a(t) = (\rho U^2/2)S\{K_a q(t) + D_a[\dot{q}(t)/U]\} \qquad (21)$$

Combining Eqs. (13, 15, 20, and 21) gives

$$\ddot{q}(t) + 2\omega \left[\zeta - \frac{B}{2\omega U}(D_s + D_a) \right] \dot{q}(t) + \omega^2 \left[1 - \frac{B}{\omega^2}(K_s + K_a) \right] q(t) = f(t) \qquad (22)$$

$$B = (\rho U^2/2)S/\bar{m} \qquad f(t) = P_b(t)/\bar{m}$$

Aerodynamic Damping

One requirement for stability is that the amplitude $|q(t)|$ is bounded, i.e., does not increase with time beyond all bounds. This implies that the coefficient for $\dot{q}(t)$ in Eq. (22) cannot be negative, i.e.,

$$\zeta - (B/2\omega U)(D_s + D_a) \geq 0 \qquad (23)$$

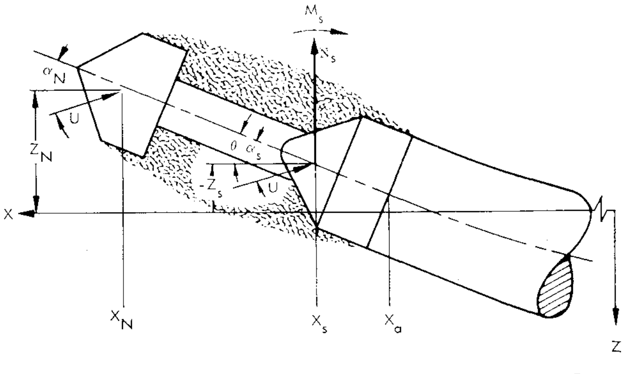

Fig. 10 Coordinate system for the elastic vehicle.

---

§ If W is the work done, $P = \partial W/\partial q$.

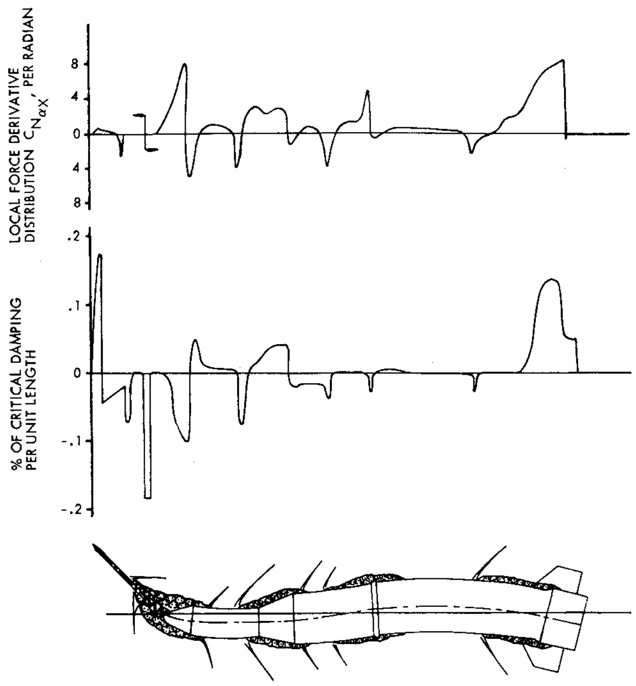

Fig. 11 Correlation of static and dynamic load distributions at $M = 1.1$ for the second bending mode of the Saturn I-Apollo with escape rocket, disk on.

In the presence of the driving function $f(t)$ the requirement of an amplitude below a certain limiting value gives a more severe criterion for stability:

$$\zeta - (B/2\omega U)(D_s + D_a) \geq \zeta_{\min} \tag{24}$$

D_s and D_a are the aerodynamic damping contributions from regions with separated and attached flow, respectively. They correspond to the damping derivative for a rigid body, a negative value indicating damped oscillation. The multiplication factor $-B/2\omega U$ brings the aerodynamic damping into the same form as the structural damping ζ. Thus, the damping contributions from the separated and attached flow regions have the following ratios to the critical damping:

$$\zeta_s = -(\rho US/4\omega\tilde{m})D_s$$

and

$$\zeta_a = -(\rho US/4\omega\tilde{m})D_a \tag{25}$$

For the lower-frequency bending modes the expression for D_s in Eq. (20) can be simplified further by approximating $\cos(\omega\Delta t) = 1$, and $\sin(\omega\Delta t) = \omega\Delta t$. In discussing the spiked body aerodynamics it was shown that $\partial C_s/\partial z = 1/L(\partial C_s/\partial\beta)$, where $L = X_N - X_s$, and $\beta = (Z_N - Z_s)/L$ (β is the angular relative deflection). The time lag Δt is determined as $\Delta t = L/\bar{U}$, where the average velocity $\bar{U}$ is determined by the velocity deficit in the wake as was discussed earlier. Using these simplifications and definitions in Eq. (20) gives the following expression for ζ_s of Eq. (25):

$$\begin{aligned}\zeta_s = \frac{\rho US}{4\omega\tilde{m}}\Bigg(\varphi(X_s)\Bigg\{&\frac{\partial C_{N_s}}{\partial\alpha_s}\varphi(X_s) + \\ &\frac{U}{\bar{U}}\left[\frac{\partial C_{N_s}}{\partial\theta_N}\varphi'(X_N)(X_N - X_s) + \frac{\partial C_{N_s}}{\partial\beta}\varphi(X_N)\right] + \\ &\frac{\partial C_{N_s}}{\partial(\dot{Z}_N/U)}\varphi(X_N)\Bigg\} + D_{\text{ref}}\,\varphi'(X_s)\left\{\frac{\partial C_{m_s}}{\partial\alpha_s}\varphi(X_s) + \right. \\ &\frac{U}{\bar{U}}\left[\frac{\partial C_{m_s}}{\partial\theta_N}\varphi'(X_N)(X_N - X_s) + \frac{\partial C_{m_s}}{\partial\beta}\varphi(X_N)\right] + \\ &\left.\left.\frac{\partial C_{m_s}}{\partial(\dot{Z}_N/U)}\varphi(X_N)\right\}\right)\end{aligned} \tag{26}$$

It has been outlined earlier how the information necessary for formulating D_s is obtained for the various types of separation. D_a is estimated by use of first-order theory.[7] The total aerodynamic damping $\zeta_s + \zeta_a$ for the elastic vehicle in single degree-of-freedom bending oscillations is obtained by summing the contributions to ζ_s and ζ_a over the vehicle.

Launch Vehicle Damping Distributions

The single degree-of-freedom damping distribution for the second bending mode at $M = 1.1$ is shown in Fig. 11. The static load distribution is also shown for reference, and the interplay between the static loads and the mode shape is clearly illustrated. In general, positive static loads contribute positive damping, and negative loads give negative damping. The exception is the separation-induced loading for the case when there is a nodal point between the separation source and the location of the separation-induced force. Then there is a sign reversal, and positive static loads contribute undamping, negative loads contribute damping. The disk wake-induced force on the command module and forward service module shows this sign reversal. The

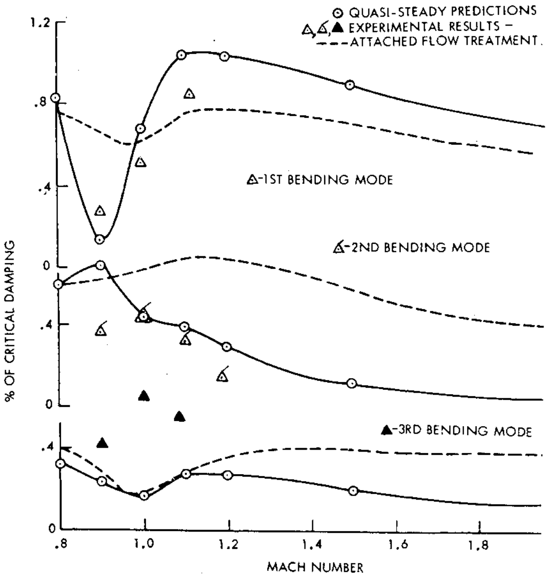

a) Disk on

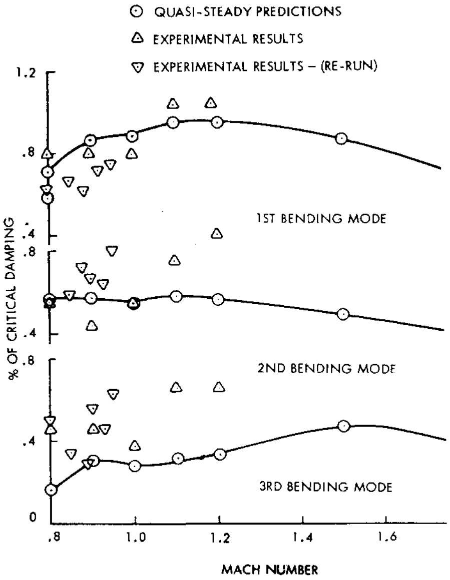

b) Disk off

Fig. 12 Aerodynamic damping at $\alpha = 0$ of the Saturn I-Apollo vehicle with escape rocket.

damping distribution, as illustrated in Fig. 11, tells the designer which characteristics in the vehicle geometry adversely affect the vehicle damping.

Comparison with Experimental Results

At the NASA Langley Research Center, Rainey[8] and others have undertaken the difficult task of simulating elastic vehicle dynamics in a wind tunnel test. An 8% dynamically scaled model of the Saturn I-Apollo vehicle was excited by an electromagnetic shaker in each of its first three bending modes, one at a time, and the aerodynamic damping was measured. In general, the quasi-steady predictions agree reasonably well with the measured damping for the three configurations tested (see Figs. 12 and 13). This is at least true for the first and second bending mode. The somewhat poor agreement for the third bending mode is probably attributable as much to the sensitivity of forebody damping to the high modal deflections and slopes as to limitations of the quasi-steady method to predict damping for the third mode because of its higher reduced frequency.¶

Treating the measured static loads as if they all were dependent only on local crossflow, as in the case of attached flow, gives obviously the wrong damping values. This is especially true for the second bending mode, where the trend with Mach number then becomes opposite to that measured. On the whole, the agreement between measured and predicted damping is acceptable considering the scatter in the experimental data.**

At the NASA Ames Research Center, Cole,[9] in his "partial-mode" testing technique, has dynamically simulated the forward portion of the Saturn I-Apollo configuration in its second bending mode. In Fig. 14a the quasi-steady prediction of the forebody damping for the second bending mode of the Langley configuration is shown for disk on and disk off. The predictions agree generally with the trends measured by Cole. The damping is positive for both configurations at subsonic speeds, whereas at supersonic speeds the disk gives a large negative damping contribution. In Fig. 14b the computed forebody damping for the tower-off configuration is shown for the second bending mode. When the loads aft of the flare are neglected, the results are comparable with the pitch damping measured on rigid bodies of similar geometry, i.e., flare-stabilized blunt-nosed cylinders. Large subsonic undamping and moderate supersonic damping are typical for these bodies. Furthermore, the alleviating effect on the undamping of an added cylindrical skirt is verified by experimental results for rigid bodies.

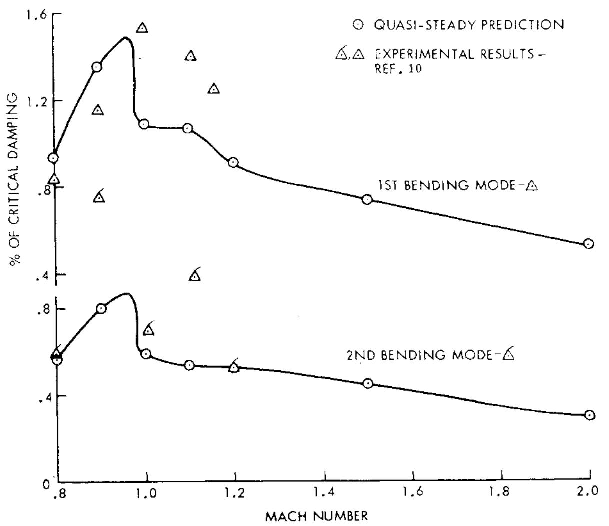

Fig. 13 Aerodynamic damping at $\alpha = 0$ of the Saturn I-Apollo vehicle without escape rocket.

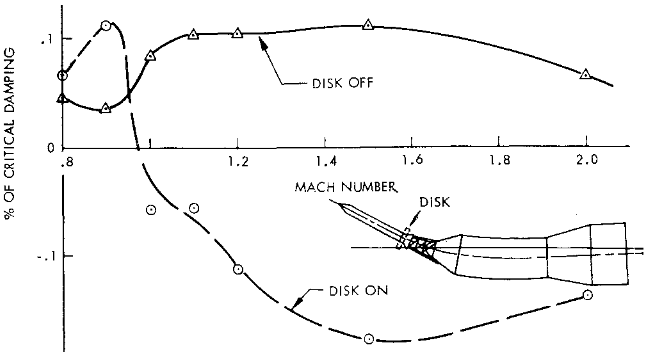

a) With escape rocket, disk on and off

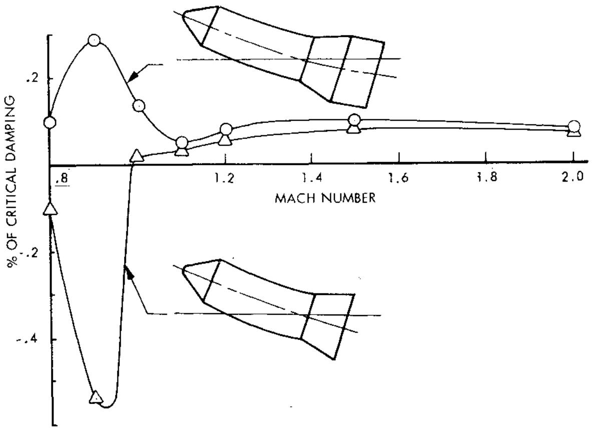

b) Without escape rocket

Fig. 14 Forebody damping at $\alpha = 0$ for the second bending mode of the Saturn-Apollo.

Conclusions

By using quasi-steady theory and experimental static data, one may successfully compute the aerodynamic damping of a vehicle that is dominated by separated flow. The damping so computed agrees well with experimental data in the transonic speed range. Whereas the supersonic damping has not been substantiated quantitatively, due to lack of experimental dynamic data, there appears to be substantial qualitative evidence supporting the predicted trends.

The results of a quasi-steady analysis of the Saturn I-Apollo vehicle reveal the following important dynamic characteristics of flow separation: 1) large regions of separated flow are capable of dominating both the static and dynamic characteristics of an elastic vehicle, and 2) the effect of mode shape is such that a sign change occurs between the separation-induced static loading and its corresponding damping contribution if a node is located between the separation source and the induced loading.

This method provides the designer with a powerful adjunct to dynamic testing, not only for the prediction of over-all vehicle damping, but also, which is more important to the designer, to show the effect on the damping of each region of flow separation.

¶ The pertinent characteristic length for the reduced frequency $(\omega d/U)$ is the local cross-sectional diameter $d \leq D_{\mathrm{ref}}$. For the third bending mode $(\omega D_{\mathrm{ref}}/U) \leq 0.75$ and the requirement for "quasi-steadiness," $(\omega d/U)^2 \ll 1$ is not satisfied over the whole vehicle.

** It should be pointed out that the total damping is the result of an ill-conditioned process of summing a number of positive and negative damping contributions (see Fig. 11), and may, therefore, be expected to be inexact. The large scatter in the experimentally measured damping (see Fig. 12) may be interpreted as evidencing the existence of the same problem when summing the contributions aerodynamically.

References

[1] Ericsson, L.-E., Woods, P., and Chavez, J. N., "A mechanism for self-excited oscillations of 'Hammerhead' and other blunt-nose missiles," *Proceedings of the 6th Symposium on Ballistic Missile and Space Technology* (Academic Press, New York, 1961), Vol. IV, pp. 68–88.

[2] Woods, P. and Ericsson, L.-E., "Aeroelastic considerations in a slender blunt-nose, multistage rocket," Aerospace Eng. **21**, 42–51 (May 1962).

[3] Reding, J. P. and Ericsson, L.-E., "Static loads on the Saturn I-Apollo launch vehicle," Lockheed Missiles and Space Company, LMSC TM 53-40-143 (LMSC-803185), Contract No. NAS 8-5338 (November 1962).

[4] Norburg, J. F. and Crabtree, L. F., "A simplified model of the incompressible flow past two-dimensional airfoils with a long bubble type of flow separation," Royal Aircraft Establishment, RAE TN Aero 2352 (June 1955).

[5] Kuehn, D. M., "Turbulent boundary-layer separation induced by flares on cylinders at zero angle of attack," NASA Ames Research Center, NASA TR R-117 (1961).

[6] Kistler, A. L. and Chen, W. S., "The fluctuating pressure field in a supersonic turbulent boundary layer," Jet Propulsion Laboratory, California Institute of Technology, TR 32-277 (August 1962).

[7] Bisplinghoff, R. L., Ashley, H., and Halfman, R. L., *Aeroelasticity* (Addison-Wesley Publishing Co., Inc., Cambridge, Mass., 1955).

[8] Rainey, G. "Progress on the launch vehicle buffeting problem," *5th Annual Structures and Materials Conference of the American Institute of Aeronautics and Astronautics* (AIAA, New York, 1964), pp. 163–177.

[9] Cole, H., Jr., Robinson, R., and Gambucci, B., "Buffeting response of the Apollo partial mode model at subsonic and supersonic Mach numbers," NASA Ames Research Center, NASA TN-D 2689 (February 1965).

JULY-AUG. 1965 J. SPACECRAFT VOL. 2, NO. 4

Laminar Boundary-Layer Growth on Slightly Blunted Cones at Hypersonic Speeds

R. E. Wilson*

U. S. Naval Ordnance Laboratory, White Oak, Silver Spring, Md.

A momentum-integral method is given for calculating the subject boundary-layer growth for the zero-angle-of-attack case. Available flat-plate boundary-layer results permit calculations for slightly blunted cones for wide ranges of hypersonic Mach number and surface temperature. Although perfect gas data are used, real gas data for equilibrium air can be introduced. Numerical results are presented for a slender cone. The results show that slight blunting greatly affects conditions at the outer edge of the boundary layer. The Mach number is markedly decreased at long distances from the tip. This is accompanied by an increase in temperature and a decrease in unit Reynolds number. The distributions through the boundary layer of parameters such as temperature and electron density will be affected. Both local skin friction and heat transfer are significantly reduced by slight blunting.

Nomenclature

a = shock radius of curvature
b = tip radius of curvature
c_f = $2\tau_w/\tau_1 u_1^2$ = local skin-friction coefficient
c_{fc} = $2\tau_w/\rho_c u_c^2$
F_1 = function defined by Eq. (13)
F_2 = function defined by Eq. (16)
H = δ^*/θ = boundary-layer shape parameter
M = Mach number
P = pressure
Pr = Prandtl number
q = local heat-transfer rate
r = local cone radius
r_s = radius of streamtube in undisturbed flow
R = Reynolds number, $R_c = \rho_c u_c x/\mu_c$, $R_{\theta c} = \rho_c u_c \theta/\mu_c$, $R_{bc} = \rho_c u_c b/\mu_c$, $R_{\theta 1} = \rho_1 u_1 \theta/\mu_1$
St = local Stanton number
T = temperature
x = distance along cone surface measured from apex
y = distance normal to surface
γ = ratio of specific heats
δ = boundary-layer thickness
$\delta^* = \int_0^\delta \left(1 - \frac{\rho u}{\rho_1 u_1}\right) dy$ = boundary-layer displacement thickness
$\theta = \int_0^\delta \left(\frac{\rho u}{\rho_1 u_1}\right)\left(1 - \frac{u}{u_1}\right) dy$ = boundary-layer momentum thickness
μ = absolute viscosity
ξ = $R_c R_{\theta c}/R_{bc}^2$
ρ = density
σ = cone half-angle
τ = shear stress
ω = shock-wave angle for sharp cone
ω_s = local shock-wave angle for blunt cone

Subscripts

c = conditions at the outer edge of the boundary layer on a sharp cone
w = conditions at the wall
l = local conditions at the outer edge of the boundary layer
∞ = freestream conditions
T = stagnation conditions

Superscripts

$'$ = reference value
0 = sharp-cone values

Received May 13, 1964; revision received September 10, 1964.

* Associate Technical Director, Aeroballistics. Associate Fellow Member AIAA.